Ocean Engineering 193 (2019) 106581

Contents lists available at ScienceDirect

Ocean Engineering

journal homepage: www.elsevier.com/locate/oceaneng

Analysis of higher harmonics in a focused water wave group by a nonlinear potential flow model

Xingya Feng [a,b,*]

[a] Department of Engineering Science, University of Oxford, Parks Road, OX1 3PJ, UK
[b] Department of Ocean Science and Engineering, Southern University of Science and Technology, Shenzhen, 518055, China

ARTICLE INFO

Keywords:
Fully nonlinear simulation
Focused wave group
Higher harmonics
Stokes expansion

ABSTRACT

This work analyses the higher harmonic wave elevations of focused wave groups based on the assumption of a Stokes-type nonlinear structure. A fully nonlinear potential flow model is employed to generate nonlinear wave groups by the NewWave theory, which represents an extreme event in a random sea state. We present a methodology to generate high-quality nonlinear wave groups of a narrow-banded wave spectrum in a numerical wave tank. A phase-manipulation approach is employed to accurately extract the higher harmonic elevations. The elevation spectra show clean separation of the first four harmonics. Comparisons with the experimental data show remarkably good agreements for the higher harmonics. We confirm the Stokes-type underlying nonlinear structure of the harmonic elevations in focused wave groups. This is found by simulating wave groups with varying wave steepness and calculating the corresponding elevation coefficients of the higher harmonics. The harmonic coefficients are found almost constant against varying steepness. An implication of the Stokes-type structure for the nonlinear wave elevations is that, it allows us to estimate the higher harmonics based only on the linear component. This is successfully demonstrated by reconstructing a nonlinear focused wave group using the linear NewWave model and the coefficients at its higher harmonics.

1. Introduction

In a random sea state, an extremely large wave will be part of a wave group, rather than in a regular wave train (Adcock and Taylor, 2009). Extreme waves are usually the most critical to the survival of offshore structures. Records of those giant waves from instruments in the ocean, for example, the well-known Draupner wave described in Walker et al. (2004), have driven extensive research on the scientific explanation of the formation of them and understanding their characteristics (Adcock et al., 2015; Wang and Balachandran, 2018). Attempt to recreate similar extreme waves in the laboratory using a deterministic wave energy spectrum has also been made in recent years such as by Buldakov et al. (2017). An engineering interest of studying the extreme waves is that these waves would produce significant nonlinear loads which could cause fatal damage to offshore structures. Understanding the characteristics of the nonlinear extreme waves improves the prediction of wave loading hence the design of offshore structures.

Extreme waves in the ocean are believed to form when the wave components associated with a large number of wave frequencies in a random sea come into phase, see a detailed explanation in Fedele et al. (2016). That is the focusing of a transient wave group. The focused wave group has been demonstrated to be the average shape of large waves in a random sea (Whittaker et al., 2016). Mathematically, the representation of the focused wave group is the scaled autocorrelation function as reported in Lindgren (1970). The simplest linear model for a focused wave group might be the NewWave presented originally in Tromans et al. (1991). The ability of the NewWave model to represent an extreme wave has been shown in a few sets of field data in deep, intermediate and shallow water depths (Walker et al., 2004; Whittaker et al., 2016; Taylor and Williams, 2004). Meanwhile, for model tests or simulations in a wave tank, an obvious advantage of using a focused wave group against a random sea state is the time savings because the focusing occurs in a very short period of time. In such a short period the near field wave is free from contamination of possible reflection from the far end of the tank.

Most of the research work mentioned above investigate the general shape of a focused wave group in the linear, or at most second order regime. It is well known that higher harmonics can be expected resulting from the strong nonlinear wave-wave interactions among the frequencies components. The nonlinear Schrödinger equation provides a

* Department of Engineering Science, University of Oxford, Parks Road, OX1 3PJ, UK.
E-mail address: fengxingya@u.nus.edu.

https://doi.org/10.1016/j.oceaneng.2019.106581
Received 16 May 2019; Received in revised form 18 September 2019; Accepted 13 October 2019
Available online 6 November 2019

good approximation for the nonlinear evolution of the wave group in deep water (Lo and Mei, 1985; Trulsen and Dysthe, 1996; Henderson et al., 1999; Adcock and Taylor, 2016). In the experimental work in Johannessen and Swan (2001) and the numerical study in Gibson and Swan (2007) and Adcock and Taylor (2016), it is shown that non-linearity in focused wave groups leads to significant changes to the shape of the groups – groups become taller and narrower with large waves moving towards the front of the groups. Nonetheless, the properties of those individual higher harmonics (than the second) remains almost unexplored due to the difficulty in accurately extracting the individual higher harmonics. There are two reasons. The first is that the higher harmonic components could be very small, for experiments possibly below the accuracy of confidence of the instruments. The second is that the higher harmonic components cannot be easily and cleanly isolated from the total nonlinear wave field due to the spectrum overlap between neighbouring orders of harmonics. Therefore, further study has to be conducted to extract cleanly the higher harmonics and to understand the nonlinear behaviour of the harmonics in an extreme wave.

Since capturing accurately the small higher harmonic elevations might be difficult in a tank test, it becomes practical to employ numerical models to replicate the process of the formation of the extreme wave. A numerical model that can simulate all nonlinearities associated with the wave group might be the time-domain fully nonlinear numerical wave tank (NWT). The NWT model we employed in this work basically represents a rectangular physical tank and simulates the wave generation and absorption. Without any assumption to the wave propagation and evolution (except for fluid viscosity), the fully nonlinear simulation will not lose any higher harmonic components arising from wave-wave interactions. Innovative approach needs to be implemented in the NWT to cleanly extract the harmonics, since we are concerned with the properties of each harmonic.

The method used in this study for decomposing higher harmonic components from a focused wave group is the phase manipulation recently presented in Adcock et al. (2019). A 'phase-inversion' or two-phase method has been adopted by Baldock et al. (1996) and Borthwick et al. (2006) for analysing the second-order wave elevations. With the two-phase method, one can obtain the odd and even harmonics by combining two realizations or response time series where the two wave groups are of 180° out of phase. Fitzgerald et al. (2014) generalized the two-phase method to a four-phase method. Similarly, the first four harmonics can be separated by combining the four wave groups of 90° phase apart. The approach assumes a Stokes-type harmonic structure of the wave elevations for a narrow-banded wave group. The regular wave amplitude A can be generalized to a time-varying amplitude $A(t)$ for the focused wave group owing to the fact that the amplitude $A(t)$ is modulated and slowly varying near focusing.

This work presents a fully nonlinear potential flow model for simulating unidirectional focused wave groups in a rectangular tank. Inviscid fluid and irrotational flow is assumed following the potential flow theory. The fully nonlinear free surface boundary conditions are fulfilled during the time-domain simulation, with the exact free surface captured in time marching. A higher order boundary element method (HOBEM) is adopted to solve the boundary value problem enclosing the fluid of interest. We generate the focused wave group from a given wave energy spectrum. Phase control is implemented at the wavemaker in order to set apart the desired wave phases. The primary purpose of this work is to investigate the characteristics of the higher harmonics in a focused wave group via clean harmonic decomposition, and to confirm the underlying structure of these harmonics. Upon confirmation of the Stokes-type nonlinear structure, the ultimate goal is to approximate the higher harmonics using the linear wave group which is simply the NewWave.

This paper is organized as follows. Section 2 briefly presents the governing equations of the nonlinear potential flow based NWT, the boundary conditions, and the boundary element method. Implementation of generating the focused wave group is also described. Section 3 focuses on validation of the numerical model by comparing with the existing experimental results. Section 4 presents the main results of this work. We first revisit the cases in Baldock et al. (1996) and use the two-phase method to extra the odd and even harmonic wave elevations. The four-phase method for extraction of the higher harmonics is then demonstrated by simulating the recent experiments. The separation is found very clean up to 4th harmonic. We confirm the Stokes-type structure of the higher order nonlinear elevations through simulations with varying wave steepness. The agreement between the fully nonlinear simulation and the test data is remarkably well. The harmonic elevation coefficients for the wave group defined similarly in the Stokes wave model are obtained. Finally, we reconstruct the higher harmonic wave elevations from the linear wave group with the obtained harmonic coefficients. Concluding remarks are drawn in the last section.

2. Mathematical formulation

2.1. Model description

We employ a numerical tank technique to simulate the focused wave groups. The rectangular numerical wave tank is defined in Fig. 1. Similar to a physical tank, a narrow long tank is modelled. The schematic figure consists of a wavemaker at the left boundary of the tank and a numerical beach placed on the surface at the far end of the tank. The coordinate system *Oxyz* has its origin on the undisturbed water surface in the centre of the tank, with z-axis pointing upward. The computational domain includes all the wetted boundaries. In particular, S_{WM} and S_F represent the wavemaker and the free water surface, respectively. It is a three-dimensional tank and the two side walls are not shown in the diagram.

The fully nonlinear potential flow theory is well established. We briefly summarize the governing equations here. On the assumptions that the fluid is incompressible and inviscid, and the flow irrotational, a scalar velocity potential $\varphi(x,y,z,t)$ can be defined, $\mathbf{u} = \nabla\varphi$, that satisfies the Laplace equation in the fluid domain,

$$\nabla^2\varphi = \frac{\partial^2\varphi}{\partial x^2} + \frac{\partial^2\varphi}{\partial y^2} + \frac{\partial^2\varphi}{\partial z^2} = 0. \tag{1}$$

For the fully nonlinear potential flow model, the fully nonlinear kinematic and dynamic conditions on the free surface S_F in the Lagrangian description are to satisfy

$$\frac{D\mathbf{X}}{Dt} = \nabla\varphi, \tag{2}$$

$$\frac{D\varphi}{Dt} = -gz + \frac{1}{2}\nabla\varphi\cdot\nabla\varphi, \tag{3}$$

where $\frac{D}{Dt} = \frac{\partial}{\partial t} + v\cdot\nabla$ is the material derivative with respect to fluid particle velocity v on the free surface, $\mathbf{X}$ denotes position of points on the free surface, and g is the gravitational acceleration. Difficulties arise to incorporate the nonlinear effects of these boundary conditions into the solution procedure. In the fully nonlinear simulation, the exact free surface has to be captured at every time step. To update the nonlinear free surface in the time domain, the Mixed Eulerian-Lagrangian (MEL) algorithm is applied in the model. The time marching scheme is the Runge-Kutta 4th order method, which has been shown numerically stable and accurate.

The boundary condition on the wavemaker S_{WM} is defined as

$$\frac{\partial\varphi}{\partial x} = U(t), \tag{4}$$

where $U(t)$ is the velocity on the wavemaker along the x direction. The velocity will be prescribed using the NewWave theory introduced later. In the model, a piston-like wavemaker is implemented. The impermeable boundary condition on side walls is

$$\frac{\partial\varphi}{\partial\mathbf{n}} = 0. \tag{5}$$

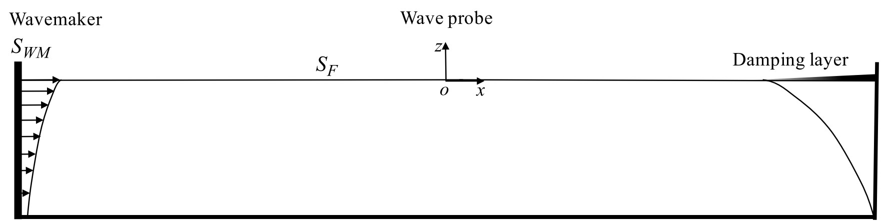

Fig. 1. Schematic diagram of a wave tank.

The numerical beach or artificial damping layer in Fig. 1 is to absorb the wave energy at the far end of the tank. In this model a simple method is adopted, i.e. modifying only the kinematic and dynamic free surface boundary conditions of Eq. (2) and Eq. (3). By adding a damping term over the damping layer length, the modified free surface boundary conditions become

$$\frac{D\mathbf{X}}{Dt} = \nabla\varphi - \nu(x_d)(\mathbf{X} - \mathbf{X}_e) \tag{6}$$

$$\frac{D\varphi}{Dt} = -gz + \frac{1}{2}\nabla\varphi\cdot\nabla\varphi - \nu(x_d)\varphi \tag{7}$$

where x_d is the distance from a point located in the damping layer to the staring point of the damping layer, $\nu(x_d)$ is the damping coefficient and $\mathbf{X}_e = (x_e, y_e, 0)$ is the reference location at the still water surface. The damping coefficient is imposed to be continuous and tuned to the peak frequency ω of the wave group. The damping coefficient is computed according to the method in Ferrant (1993).

A higher-order boundary element method is employed to solve the boundary value problem. The numerical method is briefly summarized here. The boundary integral equation (BIE) can be formulated by the Green's second identity. Considering a Green function $G(\mathbf{x}, \mathbf{x}_0)$, which is a velocity potential at a field point $\mathbf{x}_0$ due to a distributed source at $\mathbf{x}$. It satisfies the Laplace equation $\nabla^2 G = 0$ in the fluid domain except at its singular point $\mathbf{x}_0$. Applying Green's second identity by integration over the fluid domain surface enclosed by all the boundaries, we have

$$C(\mathbf{x}_0)\varphi(\mathbf{x}_0) = \iint_S \left[G(\mathbf{x}, \mathbf{x}_0)\frac{\partial\varphi(\mathbf{x})}{\partial\mathbf{n}} - \varphi(\mathbf{x})\frac{\partial G(\mathbf{x}, \mathbf{x}_0)}{\partial\mathbf{n}}\right]\mathrm{d}S \tag{8}$$

where $C(\mathbf{x}_0)$ is the solid angle at field point $\mathbf{x}_0$, and $\mathbf{n}$ is measured from the source point $\mathbf{x}$. The solid angle $C(\mathbf{x}_0)$, however, is difficult to evaluate directly. In the model we follow the treatment in Teng and Eatock Taylor (1995) who employed the physical argument that a uniform potential applied over an enclosed fluid domain produces no flux. Therefore, by considering a homogeneous Dirichlet problem where a uniform field, i.e. $\varphi = \text{constant} \neq 0$, is specified over the entire integral boundary, the above Eq. (8) becomes

$$C(\mathbf{x}_0) = -\iint_S \frac{\partial G(\mathbf{x}, \mathbf{x}_0)}{\partial\mathbf{n}}\mathrm{d}S. \tag{9}$$

In this way, the solid angle $C(\mathbf{x}_0)$ can be expressed as only a function of the boundary shape which is easily evaluated.

A simple 3D Rankine source and its image with respect to the horizontal seabed ($z = -h$) can be chosen as the Green function. The Green function is then written as

$$G(\mathbf{x}, \mathbf{x}_0) = \frac{1}{4\pi}\left(\frac{1}{R_1} + \frac{1}{R_2} + \frac{1}{R_3} + \frac{1}{R_4}\right) \tag{10}$$

where

$$\begin{cases} R_1 = \sqrt{(x-x_0)^2 + (y-y_0)^2 + (z-z_0)^2} \\ R_2 = \sqrt{(x-x_0)^2 + (y+y_0)^2 + (z-z_0)^2} \\ R_3 = \sqrt{(x-x_0)^2 + (y-y_0)^2 + (z+z_0+2h)^2} \\ R_4 = \sqrt{(x-x_0)^2 + (y+y_0)^2 + (z+z_0+2h)^2}. \end{cases} \tag{11}$$

To numerically discretize the boundaries, we introduce the shape functions $N_j(\xi, \eta)$ in each boundary element, where (ξ, η) is the local element coordinate. Thus, we are able to express the position coordinate $\mathbf{x}(\xi, \eta)$, the velocity potential $\varphi(\xi, \eta)$ and its derivatives within this element in terms of the nodal values. The boundary integral equation Eq. (8) can be written in its discretized form as

$$\begin{aligned} C(\mathbf{x}_0)\varphi(\mathbf{x}_0) = \sum_{n=1}^{N}\sum_{m=1}^{M}\Bigg\{ & G(\mathbf{x}_m, \mathbf{x}_0)\left[\sum_{j=1}^{K} N_j(\xi, \eta)\left(\frac{\partial\varphi}{\partial n}\right)_j\right] \\ & -\frac{\partial G(\mathbf{x}_m, \mathbf{x}_0)}{\partial n}\left[\sum_{j=1}^{K} N_j(\xi, \eta)\varphi_j\right]\Bigg\}\omega_m \|J_m(\xi, \eta)\| \end{aligned} \tag{12}$$

where K is the total number of nodes in the element, i.e. 6 for a triangular element and 8 for a quadrilateral element, N the total number of elements over the computational boundaries, M the number of sampling points in each element in the standard Gauss-Legendre method, ω_m the integral weight at mth sampling point, and $J_m(\xi, \eta)$ the Jacobian transformation from the global to the local coordinate. Details of calculating the integral weight and Jacobian in the standard Gauss-Legendre method can be found in Gernot et al. (2008). For each field point we have a BIE as Eq. (12). With the BIEs for all nodes on the boundaries, a linear equation system can be assembled and solved. Details about the higher-order boundary element method for solving the above boundary value problem and its numerical implementation can be found in Feng (2015).

To accelerate the computation we implement parallelization to the code using OpenMP (2015). The computational effort is mainly at assembling the dense asymmetrical matrix of influence coefficient from BIEs. The assembling has to be performed every time step as the nonlinear free surface is updated each time step. Therefore, we mainly parallelize the assembling subroutine for the influence matrix. In addition, an efficient open-source solver LAPACK (2017) is adopted to solved the linear equation system. The simulations were carried out on the high performance computing facility ARC (Richards, 2015) at the University of Oxford with multithread.

2.2. Wave generation

Key to the work here is to generate high-quality focused wave groups, as an extension of the numerical tank designed for regular waves (Bai et al., 2014; Feng and Bai, 2015, 2017). We generate a focused wave group by prescribing the proper phases of each frequency component. For a given wave energy spectrum $S(\omega)$, the free surface elevation and the velocity potential based on the linear NewWave model can be calculated as

$$\eta_I(x,t) = \sum_{n=1}^{N} A_n \cos[k_n(x-x_c) - \omega_n(t-t_c)] \quad (13)$$

$$\varphi_I(x,z,t) = \sum_{n=1}^{N} A_n \frac{\omega_n}{k_n} \frac{\cosh k_n(z+h)}{\sinh k_n h} \sin[k_n(x-x_c) - \omega_n(t-t_c)] \quad (14)$$

where A_n is the wave amplitude, ω_n the wave frequency, k_n the wavenumber of the nth component. The water depth is h. The focused time is set as t_c and the focused position x_c. The total number of component N should be large enough to reproduce the desired spectrum and $N = 200$ is adopted in this study. The amplitude $A_n(\omega)$ of each wave component is calculated by

$$A_n(\omega) = A \cdot \frac{S(\omega_n)\Delta\omega}{\sum_{n=1}^{N} S(\omega_n)\Delta\omega} \quad (15)$$

where $A = \sum_{n=1}^{N} A_n$ is defined as the linearized wave group amplitude. The NewWave profile is simply the scaled autocorrelation function, i.e. the inversed Fourier transform of the energy density spectrum for the underlying sea state, and the amplitude components are proportional to $S(\omega_n)\Delta\omega/\sigma^2$. The sum $\sigma^2 = \sum_{n=1}^{N} S(\omega_n)\Delta\omega$ is the variance of the wave elevation.

In the numerical tank as in a physical tank, to make the desired wave group, a proper transfer function $f_T(\omega)$ has to be applied to the prescribed displacement and velocity for the wavemaker. Therefore, the desired free surface elevation at the wavemaker is $\eta_I(x_{WM}, t)/ f_T(\omega)$ and the velocity distribution on the wavemaker becomes $U(t) = \frac{\partial\varphi_I(x_{WM},z,t)}{\partial x} / f_T(\omega)$ with x_{WM} the position of the wavemaker. For the piston-type wavemaker used in the model, there is a $\pi/2$ phase difference between its displacement and the wave elevation on the wavemaker. The above equations will generate waves focusing at x_c at the time instant t_c, according to linear wave theory. However, as the wave group evolution is nonlinear in this model, both the focusing location and time would slightly shift due to nonlinear dispersion and wave-wave interactions.

For decades a classic linear transfer function proposed by Ursell et al. (1960) has been used in wave generation problems. The function based on the linear wave theory is expressed as

$$f_T(\omega) = \frac{2\sinh^2 kh}{\sinh(kh)\cosh(kh) + kh}. \quad (16)$$

In our model, we compute the numerical transfer function by carrying out regular wave simulations. For a particular depth, regular waves of varying frequencies at very low amplitude ($kA < 0.01$) are generated and the transfer function is then estimated from the normalized (by the input amplitude) steady-state surface elevation. First-order position control of the wavemaker using the numerically obtained transfer function is applied in our numerical model.

A comparison of transfer functions of the numerical tank with the Ursell model is shown in Fig. 2 for the water depth 1.8 m. The difference is mostly in the frequency range 3–6 rad/s. It is established that the linear Ursell model Eq. (16) works best in shallow water regime at $kh < \pi/10$. In our case with $h = 1.8$ m, the corresponding regime of wave frequency is $\omega < 0.75$ rad/s. This is consistent with Fig. 2 that the numerically obtained function value is approaching the Ursell model when frequency becomes small. In our simulations, the input frequencies cover a range of $\omega = 1.4 - 8.1$ rad/s, in which the Ursell model is not accurate. For very short waves or higher wave frequencies, the asymptotic value for both the Ursell model and the numerical model is 2.0. The difference we see from Fig. 2 is that the numerically obtained transfer function value reaches 2.0 at a faster rate. Given the appreciable discrepancy between the numerical and the simple Ursell model, we adopt the numerically obtained transfer function in our simulations. For wave groups from a wave spectrum, a much finer frequency resolution is required between the cut-off frequencies ($0.5f_p - 3.0f_p$). A fitting function is needed to estimate the transfer function value at each frequency component discretized from the wave spectrum. Here we adopt a simple polynomial fitting at the order of 6, which works fine in the frequency range of interest, as shown in Fig. 2.

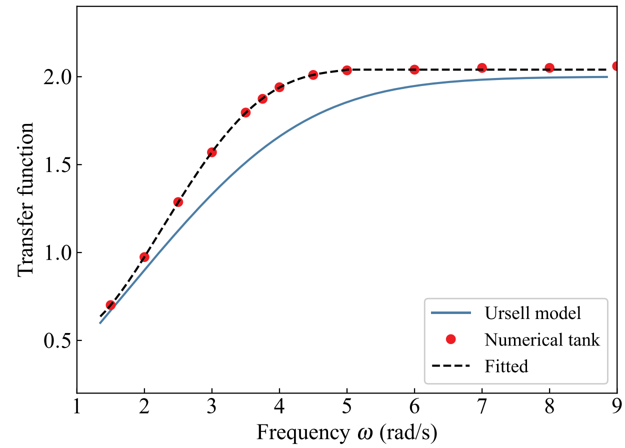

Fig. 2. Transfer function for the numerical wave tank with water depth 1.8 m.

2.3. Phase-manipulation approach

A good model for the nonlinear harmonic elevations appears to be that they follow a 'Stokes-like' form thus

$$\eta_{total} = AS_{11}\cos\phi + A^2(S_{20} + S_{22}\cos 2\phi) + A^3(S_{31}\cos\phi + S_{33}\cos 3\phi) + A^4(S_{40} + S_{42}\cos 2\phi + S_{44}\cos 4\phi) + O(A^5) \quad (17)$$

up to fourth order of the amplitude A. The coefficients S_{mn} represent the coefficients corresponding to super/sum ($m = n$) and sub/difference ($m - n = 2$) harmonics and $\phi = \omega t + \phi_0$ is the phase of the linear component of the wave. The ϕ_0 is the initial phase to be prescribed at the wavemaker. In the case of a wave group, it is assumed the time varying amplitude is modulated such that it is slowly changing near the focus time. This requires the wave spectrum to be narrow-banded (Mei et al., 2005).

To extract the different harmonics we use a phase-manipulation technique following Fitzgerald et al. (2014) who studied the wave forces on a surface-piercing column. We alter the phase at the wavemaker in certain increments. This allows us to combine different phase results in order to separate different harmonics. In particular, we make the incoming waves with a phase shift of $\phi_0 = 0°, 90°, 180°$and 270°. We then submit them into Eq. (17). By linearly combining the four corresponding responses η_0, η_{90}, η_{180} and η_{270}, the first four separated harmonics read

$$(\eta_0 - \eta_{90}^H - \eta_{180} + \eta_{270}^H)/4 = (AS_{11} + A^3S_{31})\cos\omega t, \quad (18a)$$

$$(\eta_0 - \eta_{90} + \eta_{180} - \eta_{270})/4 = (A^2S_{22} + A^4S_{42})\cos 2\omega t, \quad (18b)$$

$$(\eta_0 + \eta_{90}^H - \eta_{180} - \eta_{270}^H)/4 = A^3S_{33}\cos 3\omega t, \quad (18c)$$

$$(\eta_0 + \eta_{90} + \eta_{180} + \eta_{270})/4 = A^2S_{20} + A^4S_{40} + A^4S_{44}\cos 4\omega t. \quad (18d)$$

where the accuracy is truncated to fourth order and the superscript H denotes the Hilbert transform of the time signal. Clearly, to separate the harmonics up to fourth order using this approach, we have to repeat each simulation four times. In a relative simpler model the odd and even harmonics can be separated using only the η_0 and η_{180} signals. The averaged difference and sum of the these two signals give, up to 4th harmonic,

$$(\eta_0 - \eta_{180})/2 = (AS_{11} + A^3S_{31})\cos\omega t + A^3S_{33}\cos 3\omega t, \quad (19a)$$

$$(\eta_0 + \eta_{180}) / 2 = A^2 S_{20} + (A^2 S_{22} + A^4 S_{42}) \cos 2\,\omega t + A^4 S_{44} \cos 4\,\omega t. \tag{19b}$$

We adopt the four-phase method in this work, in order to obtain cleanly separated harmonics up to 4th order. Overlaps between the first and third, second and fourth harmonics could occur in the two-phase method, as discussed in Fitzgerald et al. (2014). For instance one has to apply a bandpass filter to further separate the $\cos \omega t$ term and the $\cos 3\,\omega t$ term from Eq. (19a). However choosing proper frequency bandwidth could be problematic when the bound harmonics associated with $\cos \omega t$ have a significant overlap with the $\cos 3\,\omega t$ component.

3. Convergence and validation

We consider the experimental investigation performed by Baldock et al. (1996) who conducted the tests in a long rectangular tank. The tank is 20 m long and 0.3 m wide with a water depth of 0.7 m. To optimise the computational efficiency, a 10 m tank is simulated in the numerical model. The origin is set at the centre of the tank, i.e. $x_c = 0.0$ m. We consider two cases in our numerical simulations, Case B and Case D which correspond to a broad-banded and narrow-banded wave spectrum, respectively. Case B has a frequency range of $f = (0.71 - 1.66)$ Hz and Case D with $f = (0.83 - 1.25)$ Hz. In each case, two amplitudes $A = 0.022$ m and $A = 0.055$ m of the wave group are simulated.

3.1. Mesh convergence

Convergence is of critical importance when it comes to the higher harmonics which is of our main concern here. The element size on the free surface shall be governed by the shortest wavelength and its higher harmonic components. We test three mesh configurations. As we simulate only unidirectional wave groups, two elements are distributed in the lateral direction. Mesh 1 corresponds to about 15 elements per shortest wavelength and Mesh 2 has nearly a twice denser mesh configuration and Mesh 3 has a total number of elements about three times that of Mesh 1. The three meshes have 6661, 11233 and 16833 nodes, respectively, distributed over the computational boundaries. It shall be reminded that higher-order elements are adopted in the model. The normalized wave elevations at the middle of the tank $x = 0.0$ m for the three mesh configurations are shown in Fig. 3(a) and the corresponding energy density spectra are displayed in Fig. 3(b). The discrepancies are almost invisible from the time histories except at some crests and troughs. One can tell the difference, however, from the energy density spectra. In order to show the small values at high frequencies, we plot the spectra in log scale. For frequencies less than 1.5 Hz, the spectra are identical for the three meshes. Relative large discrepancies appear between Mesh 1 and the other two mesh cases when $f > 1.5$ Hz. We adopt a mesh configuration similar to Mesh 2 in the following studies to compromise accuracy and computational efficiency. For the cases where a JONSWAP spectrum is used, we set the mesh density level according to the peak wavelength that dominates the wave group's main characteristics. The mesh convergence is carefully tested as well because we are aiming at capturing the very small higher harmonic components.

3.2. Effectiveness of damping zone

The effectiveness of the damping zone is governed by the long wave components in a wave group. Despite the fact that the focus time regime is very short and the reflection from the end of the tank is not critical (an important advantage of using a focused wave group), it is worthwhile to check the reflection ratio for a particular setup. As it is well known that in a physical tank the long waves are difficult to be absorbed by the damping beach, we shall see the performance of the numerical damping layer in the present model when generating wave groups. Fig. 4 shows the free surface elevations for three different setups of damping length as 1.0, 1.5 and 2.0 times the largest wavelength, λ_m. In Fig. 4(a) we can see the difference at the peaks and troughs near the focus time at $x = 0.0$ m. A closer examination reveals that the peak elevation for the damping length $1.0\lambda_m$ is over-predicted while the peaks of the damping length $1.5\lambda_m$ and $2.0\lambda_m$ are almost identical. It is clear from the elevations at the end of the tank $x = 4.9$ m in Fig. 4(c) that there is about 1% reflection for the damping length $1.0\lambda_m$ while the reflection is only 0.2% and 0.02% for $1.5\lambda_m$ and $2.0\lambda_m$, respectively. The reflected component is dominated by the wave group's main frequency. This indicates that at most the first harmonic component of the wave group would be contaminated. Nevertheless, we apply a $2.0\lambda_m$ damping zone to ensure minimum reflection.

3.3. Validation

We now compare the fully nonlinear simulations with the laboratory tests reported in Baldock et al. (1996). The time histories of the wave elevations near the focus time for the broad-banded spectrum Case B are shown in Fig. 5 with two wave amplitudes $A = 0.022$ m and $A = 0.055$ m. To demonstrate the nonlinear effect, linear prediction using the NewWave model is also included. With low wave steepness in Fig. 5(a), the numerical simulation, the measurement and the linear result are generally very close. Discrepancies arise between the linear and nonlinear results for higher steepness in Fig. 5(b). The nonlinearity clearly sharpens the crest and flattens the trough as expected. Better agreement is observed between the nonlinear model and the measured result. Note that the focus location for the steep wave is shifted downstream at around $x = 0.3$ m. The experimental observation in Baldock et al. (1996) shows constantly enlarged down shift with increasing amplitudes. The down shifting is known to be due to third-order wave-wave interactions in a wave group, and the distance of shifting depends on the nonlinearity and the spectrum bandwidth.

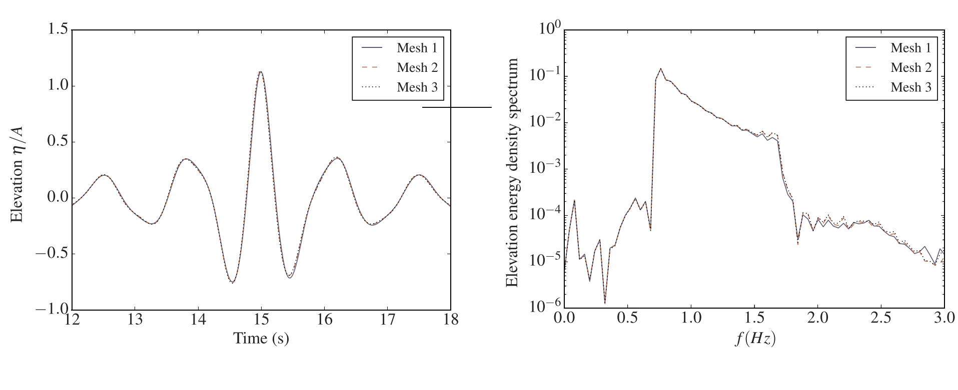

Fig. 3. Convergence of mesh for a nonlinear focused wave group at the focus point $x = 0.0$ m of Case B with $A = 0.022$ m in Baldock et al. (1996). (a) The time history and (b) the energy density spectrum.

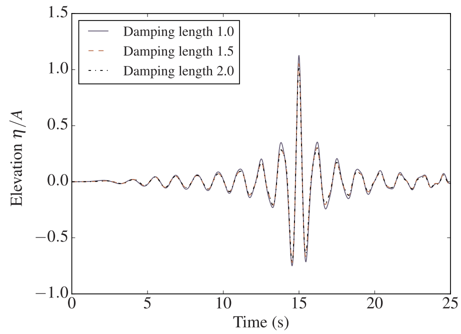

(a)

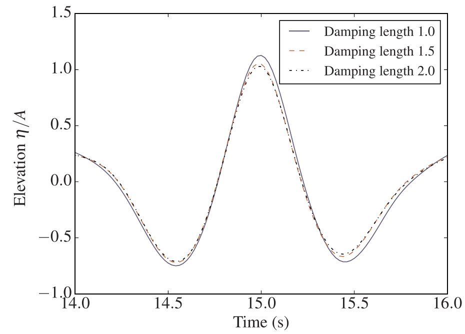

(b)

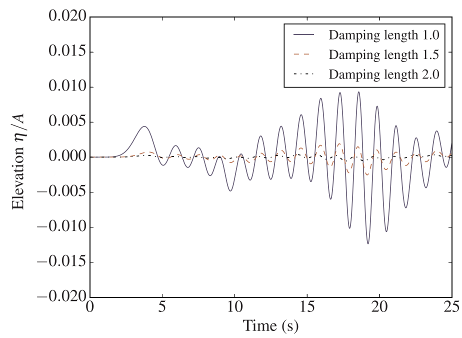

(c)

Fig. 4. Effects of different damping zone lengths on the free surface elevation at (a) $x = 0.0$ m; (b) $x = 0.0$ m near the focus time; (c) $x = 4.9$ m. Case B with $A = 0.022$ m.

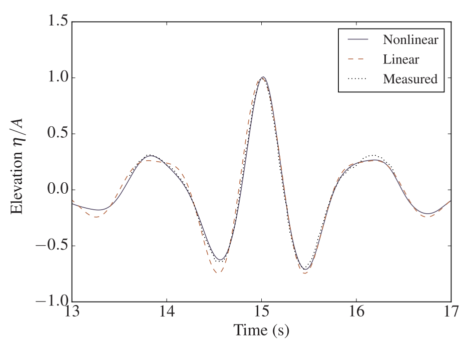

(a) $A = 0.022$ m, at $x = 0.0$ m

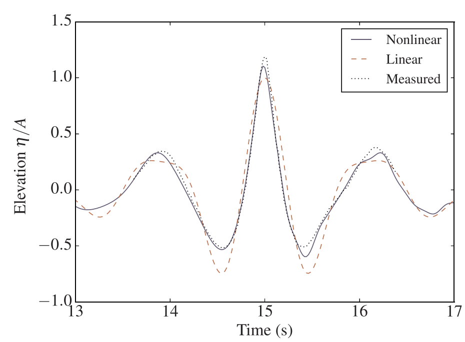

(b) $A = 0.055$ m, at $x = 0.3$ m

Fig. 5. Comparison of wave surface elevation near the focus time for Case B in Baldock et al. (1996) (a) $A = 0.022$ m, $x = 0.0$ m; (b) $A = 0.055$ m, the linear plot is at $x = 0.0$ m and the nonlinear plot is at $x = 0.3$ m.

Similar conclusions about the down shift can be drawn from the narrow-banded Case D in Fig. 6. The difference is that, as the bandwidth reduces, the shift of the focus location is more pronounced. Fig. 6(b) shows the elevations at the focus position at $x = 0.8$ m. The agreement between the numerical model and the measurement is very good, especially at the peaks and troughs. The linear model under-predicts the peak value about 30%. Nevertheless, to further confirm the accuracy of capturing the nonlinearity, one would need to compare the detailed individual harmonics at higher orders. This is one of the main objectives of this study and is demonstrated later. Here we have shown that the nonlinear numerical model is able to predict the nonlinear wave group very well, comparing with the linear model.

4. Higher harmonic analysis

The method of extracting the higher harmonics for focused wave groups is based on the phase-manipulation technique. In most of the previous studies such as in Baldock et al. (1996), Borthwick et al. (2006) and Zang et al. (2006), the two-phase or 'phase-inversion' method was used. In contrast to the four-phase method described in Eq. (18) which is used in this study, the two-phase method in Eq. (19) makes use of the time series of only the 0° and the 180° phases. The odd and even harmonic components can be separated. However, in the cases with strong wave-wave interactions the elevation energy spectrum would show overlapping between neighbouring frequencies (Fitzgerald et al., 2014). The two-phase method might not be able to separate all the harmonic components 'cleanly', thus the four-phase method is more appropriate to

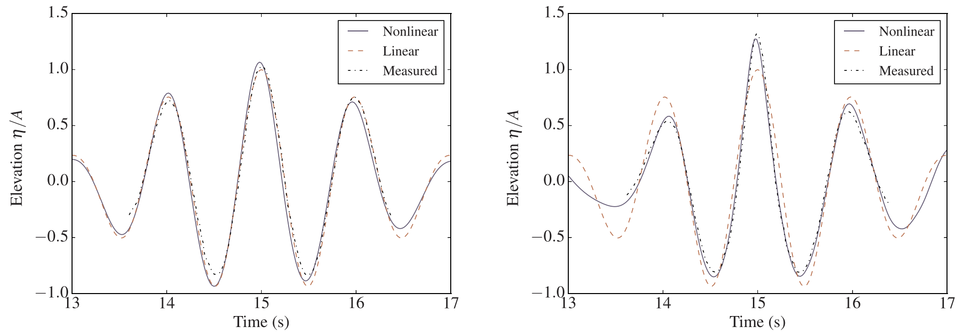

(a) $A = 0.022$ m, at $x = 0.0$ m (b) $A = 0.055$ m, at $x = 0.8$ m

Fig. 6. Comparison of wave surface elevation near the focus time for Case D in Baldock et al. (1996) (a) $A = 0.022$ m, $x = 0.0$ m; (b) $A = 0.055$ m, the linear plot is at $x = 0.0$ m and the nonlinear plot is at $x = 0.8$ m.

obtain the accurate harmonics. In the following we first present briefly the separated odd and even harmonics by the two-phase method, then we focus on demonstrating the four-phase method and clean separation of the harmonics up to fourth order.

4.1. Two-phase extraction

We take again the above cases in Baldock et al. (1996) as an example. The decomposed odd and even harmonics of elevations near focusing for Case B and Case D with $A = 0.055$ m are shown in Fig. 7(a) and (c) respectively. Their corresponding spectra are displayed on the right column. As discussed before, the nonlinearity characteristics for the narrow-banded and broad-banded spectra are different. This might be better illustrated from the separated spectra, i.e. the higher harmonic components. The spectra are plotted in log scale in order to identify clearly the energy distribution at higher harmonics. For the broad-banded Case B in Fig. 7(b), the separation seems to work well up to second order. The first harmonic in solid line is covered in the input range of (0.71–1.66) Hz with some tailing reaching 2.4 Hz. However the second harmonic in the dash line spreads in a very large frequency range, making it impossible to determine its harmonic bound. Any component above 3.0 Hz is not separated for both odd and even harmonics. For the narrow-banded Case D in Fig. 7(d), the first and third harmonics are easily identified from frequency distribution of the odd harmonics, though there might be some overlap between (2.0–3.0) Hz. The second sum harmonic becomes cleaner comparing with Case B. Ideally, the second harmonic shall cover the range of $2 \times (0.83 - 1.25)$ Hz, where (0.83–1.25) Hz is the linear range. Due to some energy

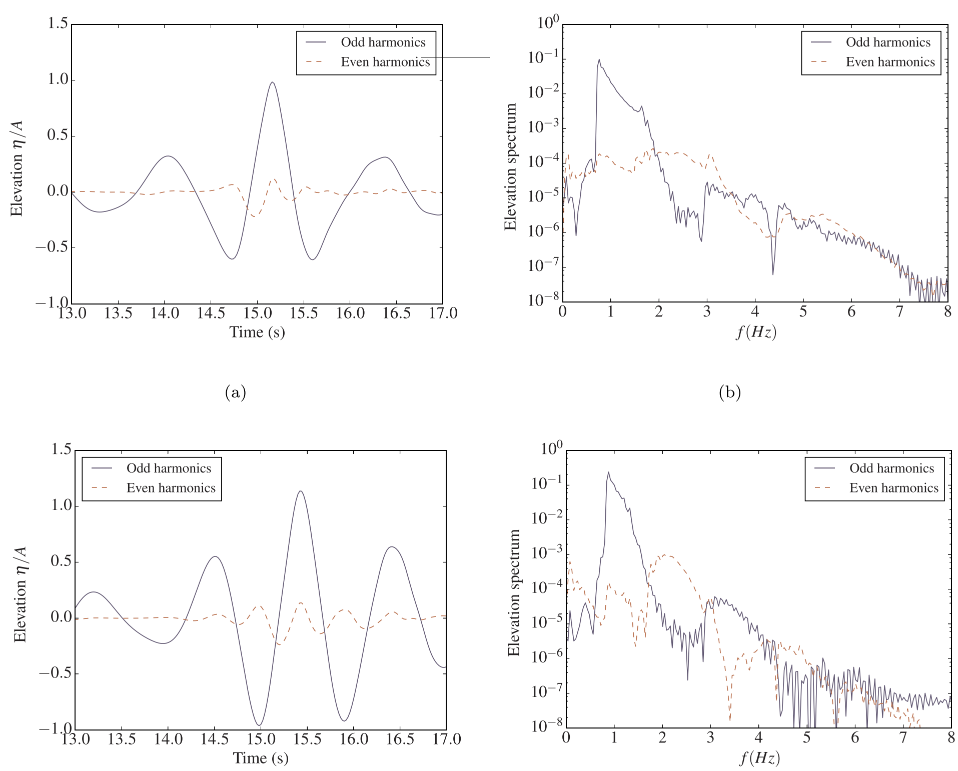

(a) (b)

(c) (d)

Fig. 7. Separation of the odd and even harmonics of the free surface elevations and their corresponding power spectra using the phase-inversion method. The top panel is for broad-banded Case B in Baldock et al. (1996) with $A = 0.055$ m at $x = 0.3$ m and the bottom panel is for narrow-banded Case D with $A = 0.055$ m at $x = 0.8$ m.

redistribution at the first harmonic (tailing), the second harmonic frequency range is slightly broadened, up to about 3 Hz. One might be able to extract the individual harmonic component by frequency filtering, with carefully selected frequency range as done in Chen et al. (2018). Nevertheless, selection of frequency filtering range can be ambiguous in many cases. In terms of harmonic separation, the phase manipulation technique seems to work better for narrow-banded spectrum. Indeed narrow-band is one of the assumptions for Stocks expanssion to be applied to focused wave groups.

4.2. Four-phase extraction

We now apply the four-phase based method to extract the harmonics. The purpose is to explore the detailed underlying structure of the higher harmonic wave elevations. We set up a tank of 15 m long and 0.2 m wide, and the water depth is 1.8 m. A narrow-banded JONSWAP spectrum is used. Its peak frequency is $f_p = 0.429$ Hz. The cutoff of input wave frequency is $0.5f_p - 3.0f_p$. The JONSWAP spectrum in this range is discretized into 200 frequency components. For a focused wave group, we use the peak wave frequency and wavelength as its characteristic property. The water depth is intermediate with $k_p h = 1.48$. Note that the Stokes wave theory breaks down at a shallow water depth. Various wave amplitudes are simulated. The setup of the case corresponds to the recent experiments conducted at the Kelvin Hydrodynamic Laboratory in the University of Strathclyde. Details about the setup of the experiments are described in the recent conference paper in Adcock et al. (2019).

The time histories of the total wave elevations for the four phases at the centre of the tank $x = 0.0$ m are shown in Fig. 8. The linear wave group amplitude is $A = 0.213$ m. The elevations are normalized by A. The linear wave group is set to focus at $t = 25$ s. The actual focus time would slightly delay and the focus location would shift downstream as discussed previously. The slight shift of focusing in time and position does not matter for the following analysis of the peak responses, because we compute the envelope of the time series instead of the maximum value. Without detailed calculation, from the figure the elevations of the four phases preserve a stable phase difference near the focus time, and they are within a same envelope as expected.

Applying the linear combinations according to Eq. (18), the resulting four time histories of the first four harmonics are shown in Fig. 10. The corresponding spectra in log scale are shown in Fig. 9. The frequency is non-dimensionalized by the peak frequency. The separation of the first four harmonics, $\eta^{(1)}$,$\eta^{(2)}$,$\eta^{(3)}$,$\eta^{(4)}$, is very successful. No overlap is present among the four. The second subharmonic or difference $\eta^{(2-)}$ covering $0-2.0f_p$ can be easily extracted from the fourth harmonic (the blue dot-dash line), as their frequency ranges are largely apart. The linear component covers the input frequency range. Higher harmonic frequencies are slightly broadened. For instance, the second sum covers the range of $1.0f_p - 5f_p$. The peak frequency of each harmonic corresponds to nf_p. For harmonics higher than 4th, the spectrum is down to the noise level and cannot be further separated.

We see from the time histories in Fig. 10 that the peaks of the higher harmonics are nicely aligned with the linear, suggesting the wave crest can be significantly enhanced if the nonlinear components are considerable. In this case, the second harmonic peak is about 20% of the linear. The third and fourth harmonics are much lower. They are really localized, appearing within about 2 s near focusing. Yet, the small higher harmonics can excite possible large resonant structural response in the environment if the offshore structure's natural frequency happens to be in this range.

Direct comparisons of the elevations, particularly the higher harmonics, are made with the experimental results. The same approach was used in the experiments to obtain the harmonics. The results for two amplitudes $A = 0.134$ m and $A = 0.213$ m are shown in Figs. 11 and 12, respectively. We shift the time histories such that the focusing time is at $t = 0.0$ s. The nth harmonics are normalized by A^n. For both cases, the linear elevations agree very well between the numerics and the experiments. The second difference $\eta^{(2-)}$ shows a significant set-down of the wave group. The numerical result in Fig. 11(b) shows the typical set-down at focusing, which is a long but smooth component. Some wavy component appears in the experimental result due to the energy 'leakage' from the linear or higher harmonics. The agreement is much better for $A = 0.213$ m in Fig. 12(b), both the trough and the overall trend.

Very good agreements are also observed in the second sum harmonics, except after the time $t = 7.0$ s when a large component appears in the numerical result. This is believed to be due to the presence of the second-order error-wave generated at the wavemaker. The presence and

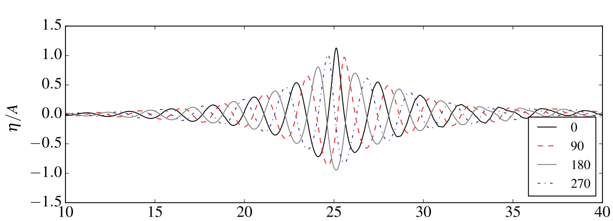

Fig. 8. Time histories of the wave elevations for four phases for $A = 0.213$ m. Te wave group has a JONSWAP spectrum with $H_S = 0.426$ m and $f_p = 0.429$ Hz.

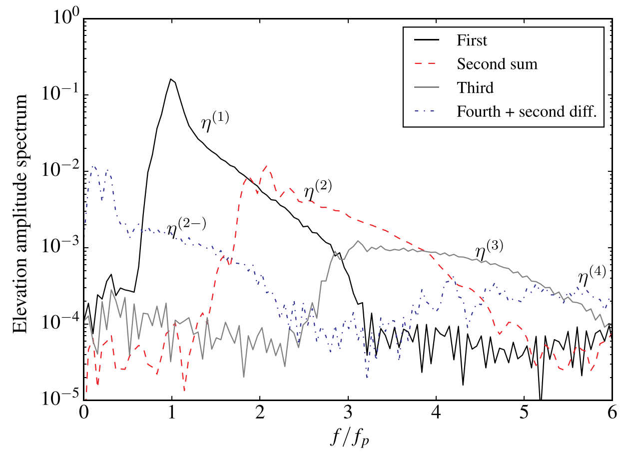

Fig. 9. Decomposed elevation spectra for $A = 0.213$ m from the four-phase method. The wave group has a JONSWAP spectrum with $H_S = 0.426$ m and $f_p = 0.429$ Hz. Input wave frequency is $0.5f_p - 3.0f_p$.

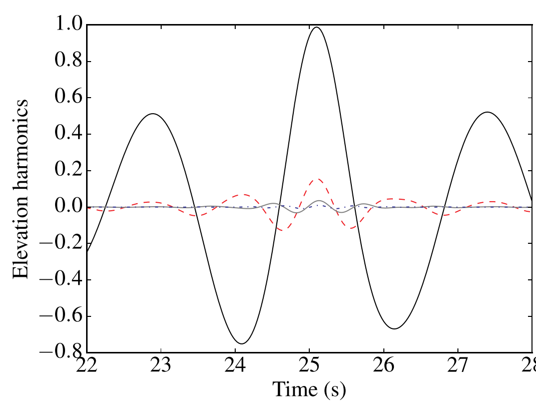

Fig. 10. Decomposed harmonic elevations for $f_p = 0.429$ Hz and $A = 0.213$ m from the four-phase method, for legend see Fig. 9.

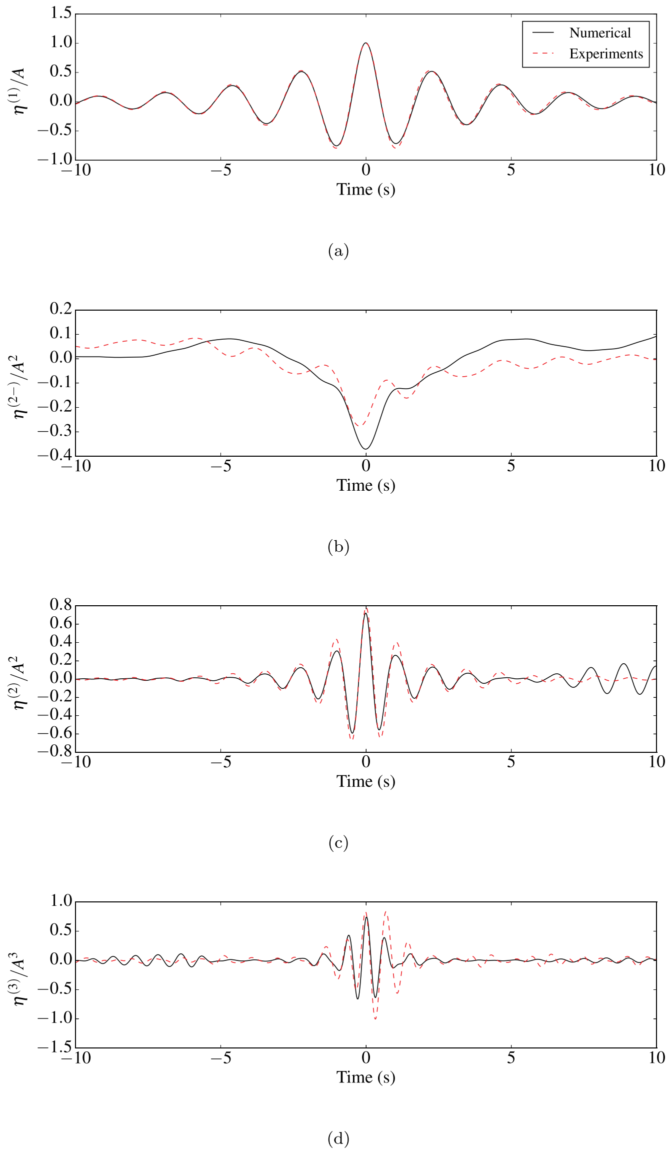

Fig. 11. Time histories of the harmonic wave elevations at the centre of the tank for $f_p = 0.429$ Hz and $A = 0.134$ m.

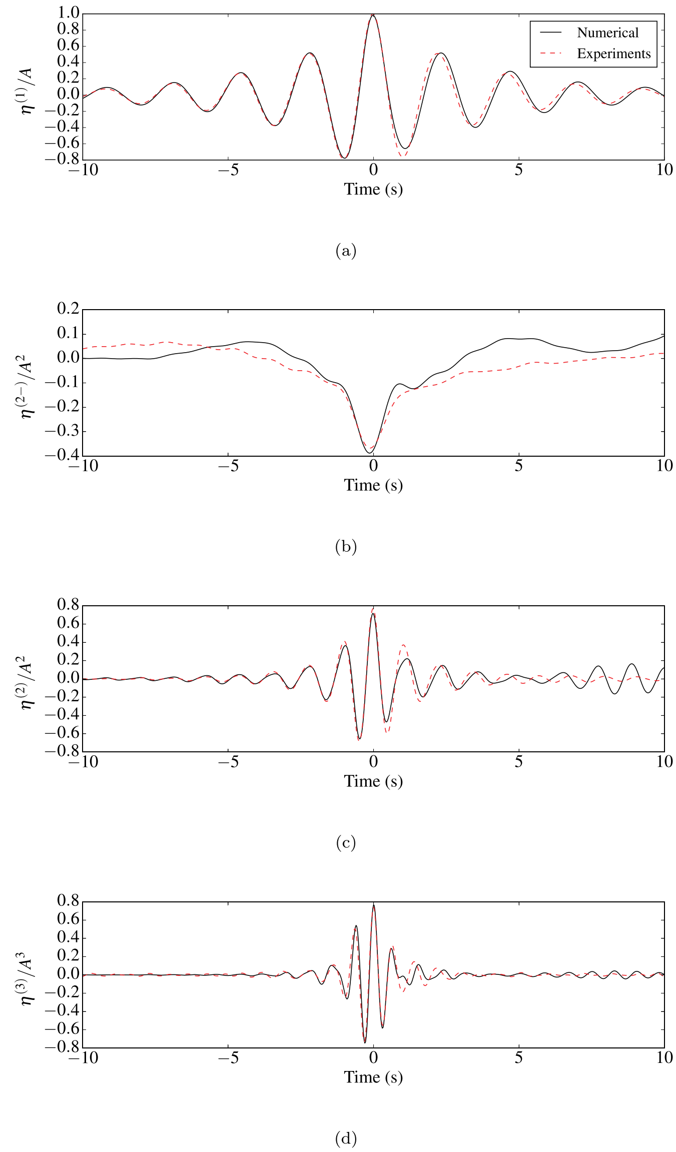

Fig. 12. Time histories of the harmonic wave elevations at the centre of the tank for $f_p = 0.429$ Hz and $A = 0.213$ m.

effect of error-wave is extensively discussed in Orszaghova et al. (2014). The source of the error-wave could be the first-order position control of the wavemaker used in the model – its effect on the second-order component was discussed in Spinneken and Swan (2009). Nevertheless, the error-wave is much delayed to the main wave group as higher frequency waves travel slower. It will not affect the magnitude of the main group. A relatively large discrepancy, particularly in phase, appears in the third harmonic in Fig. 11(d). The experimental time series seems to have a trough focus at a time instant later than $t = 0.0$ s, while the numerical result focusses at $t = 0.0$ s. The phase modification due to third-order resonant wave-wave interactions, see recently Bonnefoy et al. (2016), could be the explanation for the delay in the focused wave group. However, the discrepancy is not observed for $A = 0.213$ m in Fig. 12(d). Note that the third harmonic elevation is very small in value. Given the scrutinous comparison performed above, we are confident that the numerical model is highly accurate in predicting the higher harmonics of focused wave groups. At the same time, the four-phase decomposition approach is quite successful for the extraction of higher harmonics.

Further insight can be revealed from the time evolution of the wave profile of each harmonic along the tank in Fig. 13 where the first three harmonics are shown. This is obtained by recording the wave elevation at every point along the tank. Applying the four-phase combination method to each point gives the responses at each harmonic in the time domain. We then plot the wave profile of each harmonic along the tank at every time step. This post-processing could be time consuming, depending on the resolution of the free surface mesh. In the figures, each line shows the wave profile at a certain time step. The bold red line shows the profile at the focused time. Note that the time steps for the three harmonics are different as they evolute at different time scales. The linear wave profile in Fig. 13(a) covers a time period more than three times longer than that in Fig. 13(c). We see that the linear wave group has a smooth focusing and de-focusing process with a relatively long wavelength. In Fig. 13(b) the error-wave behind the main group is visible, in the top left triangular zone. Generally the phase speed of the second harmonic is stable. In contrast, the third harmonic profile shows some randomness of its phase over the focusing and de-focusing time period. As explained, the reason might be the underlying third-order resonant wave-wave interactions causing energy transfer between different frequency components. It is also noticed that the third harmonic component only becomes significant near the focused time and near the focused location, i.e. it is compactly localized. However, it may

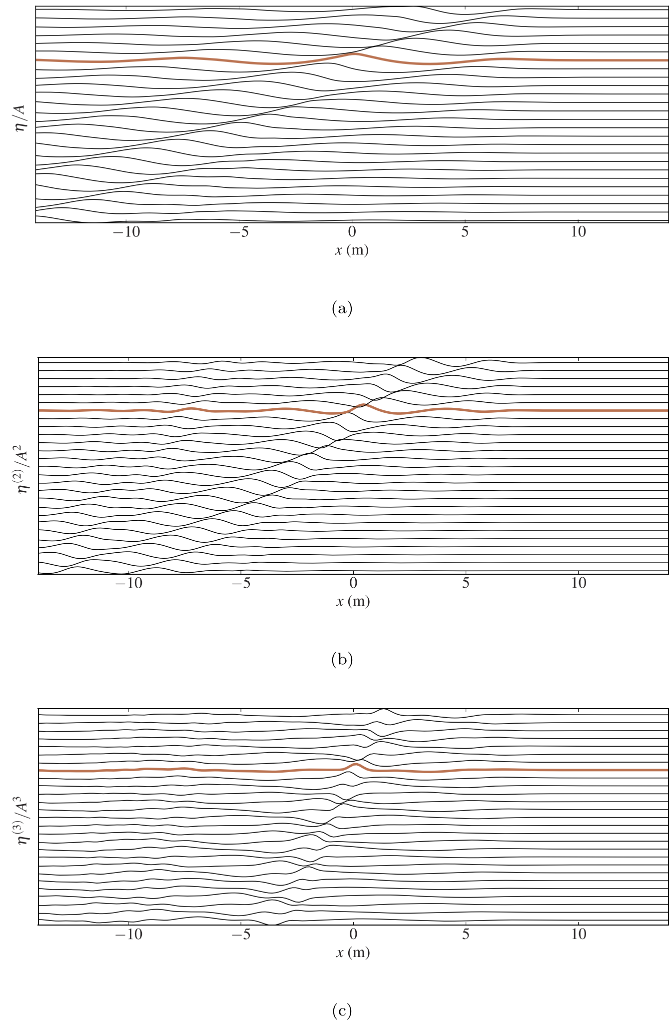

Fig. 13. Evolution of the decomposed free surface elevations along the tank with $f_p = 0.429$ Hz and $A = 0.213$ m for (a) first harmonic; (b) second harmonic; (c) third harmonic. Each line shows the wave profile at a certain time step. Time step marches from the bottom line to the top line. The bold red line shows the profile at the focused time. The time steps for the three harmonics are different as they evolute at different time scales. (For interpretation of the references to colour in this figure legend, the reader is referred to the Web version of this article.)

cause resonance if a structure is in presence which usually has a higher natural frequency than the linear frequency but near the triple frequency.

To see the separated wave profile in space clearly, we present the decomposed harmonic elevations at the focused time along the centerline of the tank in Fig. 14. We see that the second harmonic elevation in space has the same phase with the first – it sharpens the peak and flattens

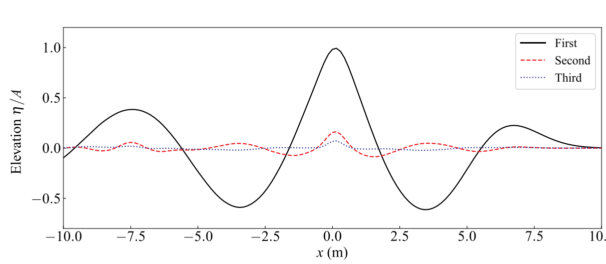

Fig. 14. Harmonic wave elevations at the focused time along the centerline of the tank for $f_p = 0.429$ Hz and $A = 0.213$ m.

the trough of the linear wave profile. The third harmonic profile is only visible near the focusing location $x = 0.0$ m.

4.3. Harmonic coefficients

In view of the 'Stokes-like' harmonics of a focused wave group in Eq. (17), we can treat the time-varying amplitude as the envelope of the time series. Using the peak value of the envelope, we are able to compute the corresponding nth harmonic coefficient as

$$S_{nn} = \frac{\max\{\Xi^{(n)}\}}{A^n} \tag{20}$$

where $\Xi^{(n)}$ is the envelope of the time series. The envelope is computed by $\Xi^{(n)} = \sqrt{(\eta^{(n)})^2 + (\eta_H^{(n)})^2}$. The subscript H represents its Hilbert transform.

To resolve the coefficient and the underlying structure of the harmonics, it is necessary to perform simulations using various wave amplitudes. Fig. 15 shows the second and third harmonic coefficients S_{22} and S_{33} against the wave steepness $k_pA = 0.05 - 0.25$. The cross is the experimental result. The short horizontal lines represent some theoretical predictions which are independent on the wave steepness. To keep the figure compact, we plot the horizontal lines over the range of $k_pA = 0 - 0.04$. In Fig. 15(a) the solid black line is the prediction using the method presented by Dalzell (1999) with modification for a wave group. The original Dalzell model considers the wave-wave interaction of two waves. We extend the model for the wave group by considering the interactions between each possible pair of wave components in the group. The modified formulation for the second-order elevation is presented in the Appendix. The dot line is simply the regular wave Stokes second-order coefficient and the dot-dash line is the Stokes coefficient in deep water. The numerical second harmonic coefficient S_{22} shows more or less a constant value about 0.74 over the steepness range. There is slight increment when the wave is steep near $k_pA = 0.20$. This trend is consistent with the experimental results, where there is minor scattering. It should be borne in mind that in the tests the actual value of the second harmonic peak is in the level of millimetre or smaller, which is to the accuracy of wave gauges. For the numerical model, probing the small wave elevations is not an issue. The averaged numerical S_{22} agrees very well with the modified Dalzell model, and both are about 10% higher than the Stokes coefficient. The corresponding coefficient in deep water $S_{22} = \frac{1}{2}k_p$ is much lower. This is expected since the wave nonlinearity typically weakens with the increase of water depth.

The third harmonic coefficient S_{33} of the experiments is more scattering than the second. The scattering seems to occur either at low steepness or high steepness ranges. For the very mild wave, possibly the wave gauges could not capture the tiny component at the third harmonic. For the relatively steep wave, the third-order resonant wave-wave interaction would occur, breaking down the 'Stokes-like' nonlinear structure. Nonetheless, the numerical results are still constant against the steepness. Again, the averaged numerical coefficient S_{33} is close to that of the experiments. The regular wave Stokes third-order coefficient underestimates the test results by about 30%. Though close, in any case the focused wave group is different from a regular wave. The nonlinear wave-wave interaction could play an important role in modifying the peak or trough of a focused wave group, especially the third harmonic.

It might be interesting to study the variation of the harmonic coefficient against the wavenumber at a constant water depth. The second harmonic coefficient as a function of k_ph is depicted in Fig. 16. Here we investigate three water depths, i.e. $h = 0.5$ m, 1.8 m, 10 m. In each figure, we plot results of the numerical model, the modified Dalzell model and the Stokes coefficient. For the small water depth in Fig. 16(a), we see a significant drop of S_{22} when $k_ph < 1.0$ at shallow-water regime. The numerical result seems to be between the Dalzell's and the Stokes

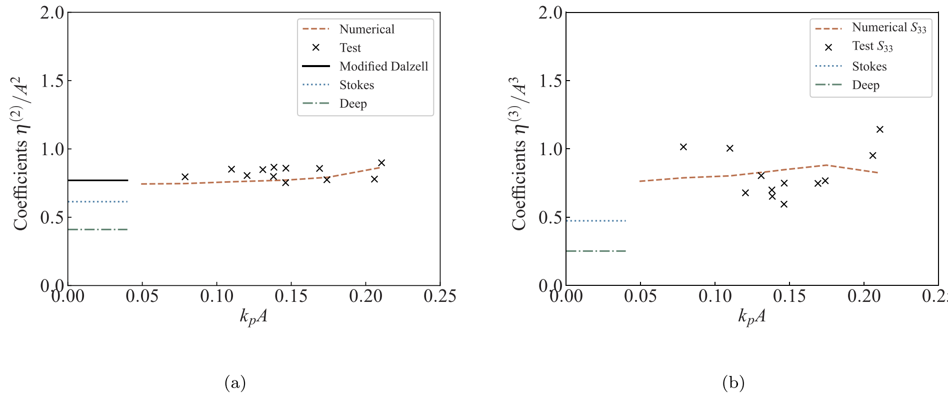

Fig. 15. Harmonic coefficients of wave elevations for focused wave groups for $f_p = 0.429$ Hz with comparison against tests. The short horizontal lines are the theoretical predictions which are constants across k_pA.

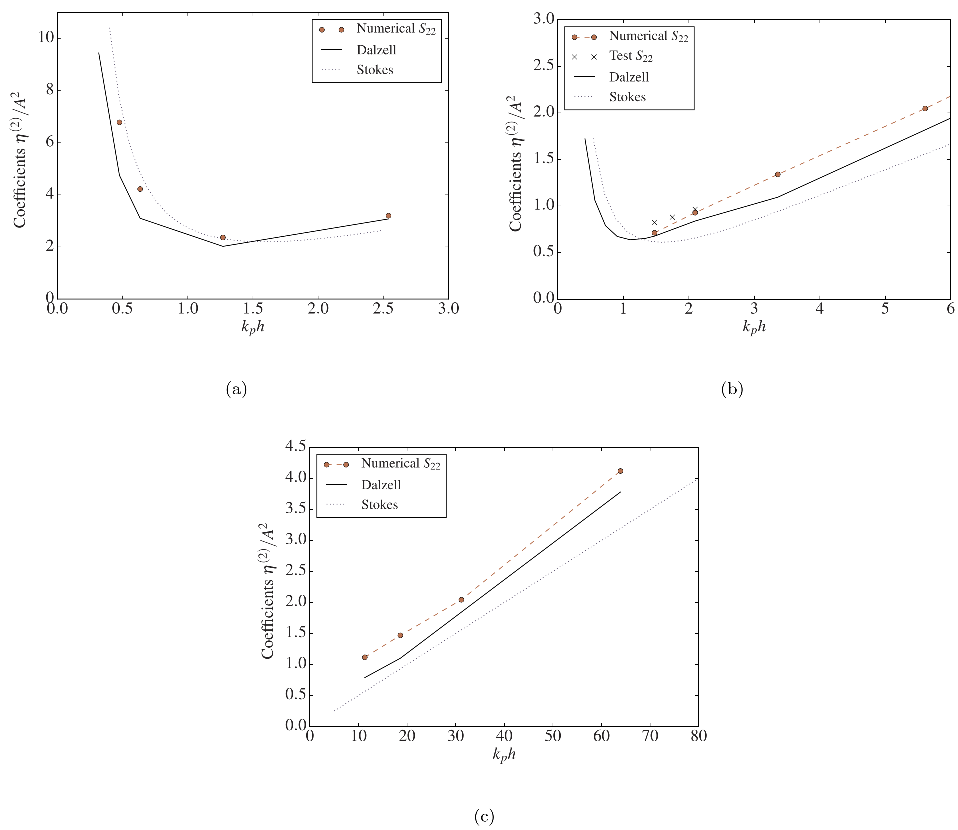

Fig. 16. Harmonic coefficients of second-order elevation for varying peak frequency at three water depths (a) $h = 0.5$ m; (b) $h = 1.8$ m; (c) $h = 10$ m.

coefficients, with the Stokes coefficient slightly higher than the other two. The trend however changes when $k_ph > 1.5$. The Stokes coefficient is slightly lower. There is an intersection near $k_ph = 1.5$, and similar intersection is present for the 1.8 m depth case in Fig. 16(b). In deep water, the coefficient increases almost linearly with k_ph. The discrepancies among the numerical results, Dalzell's model and Stokes seem consistent. The same conclusion can be drawn from Fig. 16(c) with $h = 10$ m. It is worthy pointing out that we use a wave steepness about $k_pA = 0.1$ for the numerical simulations. The second-order coefficient is in the order of A^2.

4.4. Estimation of higher harmonics from linear wave

A primary purpose of obtaining the harmonic coefficients is to estimate the higher harmonics using the time series of the linear wave elevation $\eta^{(1)}$. The total wave elevation can be approximated as

$$\eta = \eta^{(1)} + S_{22}A^2\left[\left(\eta^{(1)}\right)^2 - \left(\eta_H^{(1)}\right)^2\right] + S_{33}A^3\left[\left(\eta^{(1)}\right)^3 - 3\eta^{(1)}\left(\eta_H^{(1)}\right)^2\right]$$
$$+ S_{44}A^4\left[\left(\eta^{(1)}\right)^4 - 6\left(\eta^{(1)}\eta_H^{(1)}\right)^2 + \left(\eta_H^{(1)}\right)^4\right] \quad (21)$$

We take the case where $f_p = 0.429$ Hz and $A = 0.213$ m as an example. We compute the harmonic coefficient S_{nn} according to Eq. (20) up to 5th order. The 'Stokes-type' structure indicates the harmonic component shall have the form $\hat{\eta}^{(n)} = A^n S_{nn}\cos(n\omega t + \varphi_n)$, where $A(t)$ is the linear amplitude (In practice, this can be obtained from the New-Wave model) and φ_n is the phase of the harmonic response. Note that the coefficient S_{nn} is not a function of the wave steepness. Estimation of $\cos(n\omega t + \varphi_n)$ for each higher harmonic from the linear $\eta^{(1)}$ and its Hilbert transform $\eta_H^{(1)}$ is documented in the Appendix in Walker et al.

(2004).

The estimated time series of the harmonic elevations are shown in Fig. 17. The solid line is the direct results from the numerical simulation and the dash line is estimated using the reconstruction model Eq. (21). The harmonic coefficients S_{nn} utilized in the reconstruction model are obtained from the numerical simulation. They are the averaged S_{nn} over the varying k_pA. We see that the overall reconstruction is successful up to 5th harmonic. The total elevation is well estimated. Small discrepancy appears at the second harmonic near the focus time. However, the possible error-wave after 30 s cannot be captured. This is not a surprise because the reconstructed higher harmonic elevations will not have any 'wiggle' following the main group. The reconstructed harmonics are also more symmetric about the focus time than the original extracted ones, because the linear component is essentially symmetric. From the total elevation, we see that the reconstructed elevation is almost identical to the original, except for the small discrepancy after 30 s which is due to the presence of the second-order error-wave. Again, the higher harmonic components above the third order are generally very small. Some noise seems to appear in the fifth harmonic. Nevertheless, we can reconfirm the underlying 'Stokes-type' structure of the nonlinear harmonics. We demonstrate that it is possible to estimate the higher harmonics of a focused wave group by its linear wave elevation with the harmonic coefficients.

5. Concluding remarks

We present a fully nonlinear potential flow model with implementation of generation of focused wave groups. A phase-manipulation method is adopted to decompose the harmonic components of the nonlinear wave elevation. Mesh convergence at the higher harmonics is carefully carried out. The four-phase method is demonstrated successful for separating the higher harmonics in the nonlinear wave group.

Direct comparison of the harmonic time histories is made with the recent experiments. The agreement is generally good. The second harmonic from the numerical model shows a 'secondary' group following the main group, which however is not present in the experiment. It is believed to be the effect of error-wave of the second order. The error-wave is much delayed and has no influence on the main group. Small discrepancies are also observed in the third harmonic elevation. While the third harmonic peak values are close for the numerical and experimental results, there exists a slight phase difference. This is explained by the phase modification resulting from resonant third-order wave-wave interactions, which may not be captured in the numerical model. Nevertheless, the absolute higher harmonic components are very small. The differences are not visible from the total elevations.

The evolution of the decomposed higher harmonic wave profile is illustrated. Both the linear and second harmonics show smooth profiles along the tank. The third is localized and wavy due to its short wave length and possible phase modification.

To confirm the Stokes-like structure of the higher harmonics, we simulate the wave groups with varying amplitudes. We compare the harmonic coefficients with both the tests and the theory at increasing wave steepness. The second-order coefficient S_{22} is almost constant against the steepness for the numerical results. Small variation is present in the test data. The second-order wave-wave interaction model by Dalzell (1999) is extended for a focused wave group. The modified Dalzell model shows good prediction, while the Stokes second-order model (for regular waves) slightly under-predicts the second-order coefficient. For the third-order coefficient S_{33}, the numerical results are almost constant with increasing wave steepness while the variation in the test data is considerable, especially when the steepness is either low or high. Again, the Stokes third-order model under-predicts S_{33}.

With the harmonic coefficients up to fifth order, we estimate the higher harmonics from the linear elevation. The reconstructed elevations agree well with the original, confirming again the Stokes-type structure for the higher harmonics. The harmonic component coefficients are not a function of the wave steepness, suggesting one can estimate the harmonics from only the simple linear model for both mild and steep waves. While the second harmonic coefficient for the focused wave group can be directly computed from the extended Dalzell model, higher harmonic coefficients for any general case cannot be easily obtained, except running nonlinear simulations. Future investigations would be made to study the wave-wave interactions at the third and higher orders, leading to the quick estimation of the harmonic coefficients.

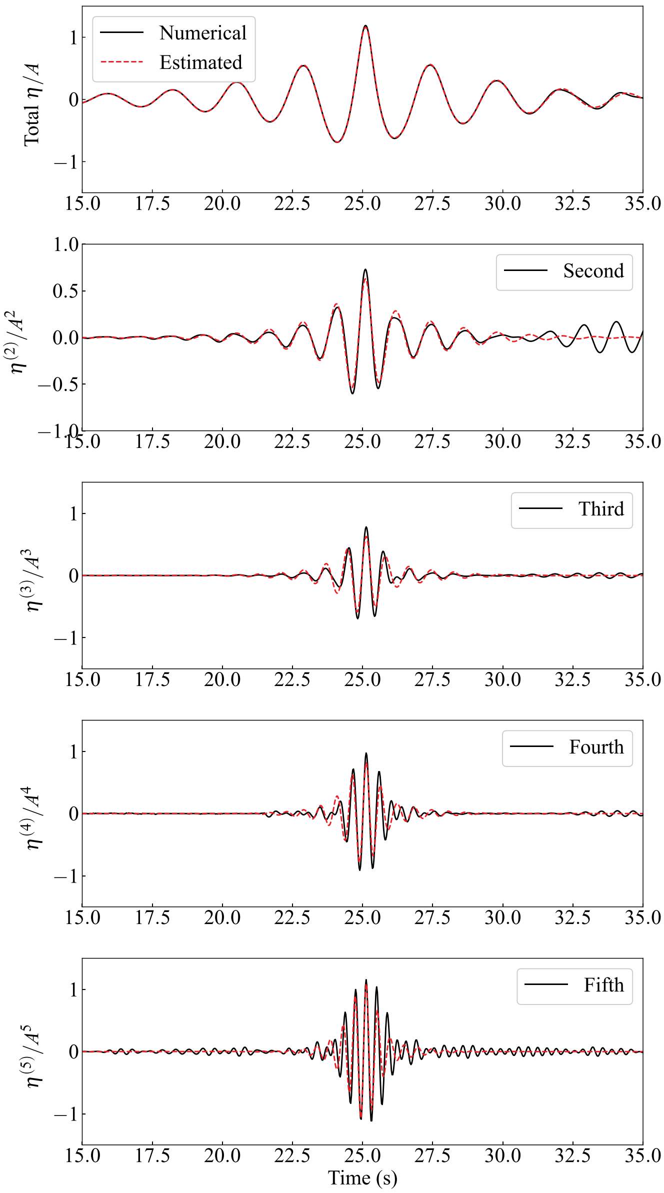

Fig. 17. Reconstructed harmonic elevations for $f_p = 0.429$ Hz and $A = 0.213$ m using averaged coefficients obtained from the present numerical model. The $n$the harmonic elevation is non-dimensionalized by A^n.

Acknowledgements

This work was funded by UK/China Offshore Renewable Energy funding (EPSRC grant EP/R007632/1). The author would like to acknowledge the comments from Professor Thomas Adcock at the University of Oxford. The author would also like to acknowledge the use of the University of Oxford Advanced Research Computing (ARC) facility in carrying out the numerical work.

Appendix

The mathematical model of second-order wave-wave interaction for two regular waves was presented by Dalzell (1999). We modify it for a focused wave group in a random sea state. This is done by considering every pair of two components in a wave group and summing up all the possible pairs. The formulation in Dalzell (1999) considers directional spreading. Here we set up the direction of all the wave component as zero, making it uni-directional. The regular wave-wave interaction resulting from two components in uni-direction has the second-order sum elevation

$$\eta^{(22)} = \frac{A_1^2 k_1}{4\tanh k_1 h}\left[2 + \frac{3}{\sinh^2(k_1 h)}\right] + \frac{A_2^2 k_2}{4\tanh k_2 h}\left[2 + \frac{3}{\sinh^2(k_2 h)}\right] + A_1 A_2 B_p \tag{A.1}$$

$$\begin{aligned} B_p = \frac{\omega_1^2 + \omega_2^2}{2g} - \frac{\omega_1\omega_2}{2g}\left[1 - \frac{1}{\tanh k_1 h\,\tanh k_2 h}\right] \times \left[\frac{(\omega_1+\omega_2)^2 + g(k_1+k_2)\tanh(k_1 h + k_2 h)}{D_p}\right] \\ + \frac{\omega_1+\omega_2}{2gD_p}\left[\frac{\omega_1^3}{\sinh^2(k_1 h)} + \frac{\omega_2^3}{\sinh^2(k_2 h)}\right] \end{aligned} \tag{A.2}$$

$$D_p = (\omega_1+\omega_2)^2 - g(k_1+k_2)\tanh(k_1 h + k_2 h) \tag{A.3}$$

where the subscript 1 and 2 stand for the quantities associated with the two wave components. $A_{1,2}$ are the amplitudes, $\omega_{1,2}$ the frequencies, g the gravitational acceleration and h the water depth. Each wavenumber $k_{1,2}$ still satisfies the linear dispersion equation $\omega_{1,2}^2 = gk_{1,2}\tanh(k_{1,2}h)$. Note that here only the second harmonic elevation is resolved from Dalzell's result. The difference term and the mean elevation term are not included.

In the focused wave group, as the phases of all components are aligned, the amplitude of the second-order wave elevation will be the summation of the elevations resulting from interactions between every two components. We have the following second harmonic elevation for the wave group

$$\eta_{group}^{(22)} = \sum_{j=1}^{N}\sum_{k=j}^{N}\eta_{jk}^{(22)} \tag{A.4}$$

where N is the total number of components in the wave group and j, k are the indexes of any two components.

References

Adcock, T.A.A., Feng, X., Tang, T., van den Bremer, T.S., Day, A.H., Dai, S., Li, Y., Lin, Z., Xu, W., Taylor, P.H., 2019. Application of phase decomposition to the analysis of random time series from wave basin tests. In: Proceedings of the ASME 2019 38th International Conference on Ocean, Offshore and Arctic Engineering. American Society of Mechanical Engineers.

Adcock, T.A.A., Taylor, P.H., 2009. Focusing of unidirectional wave groups on deep water: an approximate nonlinear Schrödinger equation-based model. Proc. R. Soc. A Math. Phys. Eng. Sci. 465, 3083–3102. https://doi.org/10.1098/rspa.2009.0224.

Adcock, T.A.A., Taylor, P.H., 2016. Non-linear evolution of uni-directional focussed wave-groups on a deep water: a comparison of models. Appl. Ocean Res. 59, 147–152. https://doi.org/10.1016/j.apor.2016.05.012.

Adcock, T.A.A., Taylor, P.H., Draper, S., 2015. Nonlinear dynamics of wave-groups in random seas: unexpected walls of water in the open ocean. Proc. R. Soc. A Math. Phys. Eng. Sci. 471 https://doi.org/10.1098/rspa.2015.0660.

Bai, W., Feng, X., Eatock Taylor, R., Ang, K.K., 2014. Fully nonlinear analysis of near-trapping phenomenon around an array of cylinders. Appl. Ocean Res. 44, 71–81. https://doi.org/10.1016/j.apor.2013.11.003.

Baldock, T.E., Swan, C., Taylor, P.H., 1996. A laboratory study of nonlinear surface waves on water. Phil. Trans. R. Soc. Lond. A: Math., Phys. Eng. Sci. 354, 649–676. https://doi.org/10.1098/rsta.1996.0022.

Bonnefoy, F., Haudin, F., Michel, G., Semin, B., Humbert, T., Aumaitre, S., Berhanu, M., Falcon, E., 2016. Observation of resonant interactions among surface gravity waves. J. Fluid Mech. 805, R3. https://doi.org/10.1017/jfm.2016.576.

Borthwick, A.G.L., Hunt, A.C., Feng, T., Taylor, P.H., Stansby, P.K., 2006. Flow kinematics of focused wave groups on a plane beach in the U.K. Coastal Research Facility. Coast. Eng. 53, 1033–1044.

Buldakov, E., Stagonas, D., Simons, R., 2017. Extreme wave groups in a wave flume: controlled generation and breaking onset. Coast. Eng. 128, 75–83. https://doi.org/10.1016/j.coastaleng.2017.08.003.

Chen, L.F., Zang, J., Taylor, P.H., Sun, L., Morgan, G.C.J., Grice, J., Orszaghova, J., Tello Ruiz, M., 2018. An experimental decomposition of nonlinear forces on a surface-piercing column: Stokes-type expansions of the force harmonics. J. Fluid Mech. 848, 42–77. https://doi.org/10.1017/jfm.2018.339.

Dalzell, J., 1999. A note on finite depth second-order wave-wave interactions. Appl. Ocean Res. 21, 105–111.

Fedele, F., Brennan, J., Ponce de León, S., Dudley, J., Dias, F., 2016. Real world ocean rogue waves explained without the modulational instability. Sci. Rep. 6, 27715. https://doi.org/10.1038/srep27715.

Feng, X., 2015. Hydrodynamic Analysis of Wave Interactions with Marine Multibody Systems. PhD thesis. National University of Singapore, Singapore.

Feng, X., Bai, W., 2015. Wave resonances in a narrow gap between two barges using fully nonlinear numerical simulation. Appl. Ocean Res. 50, 119–129. https://doi.org/10.1016/j.apor.2015.01.003.

Feng, X., Bai, W., 2017. Hydrodynamic analysis of marine multibody systems by a nonlinear coupled model. J. Fluids Struct. 70, 72–101. https://doi.org/10.1016/j.jfluidstructs.2017.01.016.

Ferrant, P., 1993. Three-dimensional unsteady wave-body interactions by a Rankine boundary element method. Ship Technol. Res. 40, 165–175.

Fitzgerald, C.J., Taylor, P.H., Taylor, R.E., Grice, J., Zang, J., 2014. Phase manipulation and the harmonic components of ringing forces on a surface-piercing column. Proc. R. Soc. Lond.: Math., Phys. Eng. Sci. 470 https://doi.org/10.1098/rspa.2013.0847.

Gernot, B., Ian, M.S., Christian, D., 2008. The Boundary Element Method with Programming for Engineers and Scientists. Springer.

Gibson, R., Swan, C., 2007. The evolution of large ocean waves: the role of local and rapid spectral changes. Proc. R. Soc. A Math. Phys. Eng. Sci. 463, 21–48. https://doi.org/10.1098/rspa.2006.1729.

Henderson, K., Peregrine, D., Dold, J., 1999. Unsteady water wave modulations: fully nonlinear solutions and comparison with the nonlinear Schrodinger equation. Wave Motion 29, 341–361. https://doi.org/10.1016/S0165-2125(98)00045-6.

Johannessen, T., Swan, C., 2001. A laboratory study of the focusing of transient and directionally spread surface water waves. Proc. R. Soc. Lond. Ser. A: Math., Phys. Eng. Sci. 457, 971–1006. https://doi.org/10.1098/rspa.2000.0702.

LAPACK, 2017. LAPACK–Linear Algebra PACKage. http://www.netlib.org/lapack.

Lindgren, G., 1970. Some properties of a normal process near a local maximum. Ann. Math. Stat. 1870–1883.

Lo, E., Mei, C.C., 1985. A numerical study of water-wave modulation based on a higher-order nonlinear Schrödinger equation. J. Fluid Mech. 150, 395–416. https://doi.org/10.1017/S0022112085000180.

Mei, C.C., Stiassnie, M., Yue, D.K.P., 2005. Theory and Applications of Ocean Surface Waves, vol. 23. World Scientific.

OpenMP, 2015. OpenMP API 4.5 Fortran Syntax Reference Guide. https://www.openmp.org.

Orszaghova, J., Taylor, P.H., Borthwick, A.G.L., Raby, A.C., 2014. Importance of second-order wave generation for focused wave group run-up and overtopping. Coast. Eng. 94, 63–79.

Richards, A., 2015. University of Oxford Advanced Research Computing. https://doi.org/10.5281/zenodo.22558.

Spinneken, J., Swan, C., 2009. Second-order wave maker theory using force-feedback control. Part I: a new theory for regular wave generation. Ocean Eng. 36, 539–548. https://doi.org/10.1016/j.oceaneng.2009.01.019.

Taylor, P.H., Williams, B.A., 2004. Wave statistics for intermediate depth water–NewWaves and symmetry. J. Offshore Mech. Arct. Eng. 126, 54–59. https://doi.org/10.1115/1.1641796.

Teng, B., Eatock Taylor, R., 1995. New higher-order boundary element methods for wave diffraction/radiation. Appl. Ocean Res. 17, 71–77.
Tromans, P.S., Anaturk, A.R., Hagemeijer, P., 1991. A new model for the kinematics of large ocean waves-application as a design wave. In: The First International Offshore and Polar Engineering Conference. International Society of Offshore and Polar Engineers.
Trulsen, K., Dysthe, K.B., 1996. A modified nonlinear Schrödinger equation for broader bandwidth gravity waves on deep water. Wave Motion 24, 281–289. https://doi.org/10.1016/S0165-2125(96)00020-0.
Ursell, F., Dean, R.G., Yu, Y.S., 1960. Forced small-amplitude water waves: a comparison of theory and experiment. J. Fluid Mech. 7, 33–52. https://doi.org/10.1017/S0022112060000037.
Walker, D.A.G., Taylor, P.H., Eatock Taylor, R., 2004. The shape of large surface waves on the open sea and the Draupner New Year wave. Appl. Ocean Res. 26, 73–83.
Wang, R., Balachandran, B., 2018. Extreme wave formation in unidirectional sea due to stochastic wave phase dynamics. Phys. Lett. A 382, 1864–1872. https://doi.org/10.1016/j.physleta.2018.04.050.
Whittaker, C., Raby, A., Fitzgerald, C., Taylor, P., 2016. The average shape of large waves in the coastal zone. Coast. Eng. 114, 253–264. https://doi.org/10.1016/j.coastaleng.2016.04.009.
Zang, J., Gibson, R., Taylor, P.H., Eatock Taylor, R., Swan, C., 2006. Second order wave diffraction around a fixed ship-shaped body in unidirectional steep waves. J. Offshore Mech. Arct. Eng. 128, 89–99.